From (A.3) and (A.4) we have the identity

$$(\zeta''/\zeta P) = -(1/12)\left[d^2\left((\chi')^2/(b-\chi(y))^{1/2}\right)/db^2 \right]_{b=b_n^{(1)}} + (1/4)d(\chi'/P^3)/dy - (1/2)\eta'(\mu_n-\eta^2)^{-3/2} - (5/4)\eta^2\eta'(\mu_n-\eta^2)^{-5/2}.$$

Using this identity, we can easily obtain the relation

$$\int_{y^1+\delta}^{y^2-\delta}(\zeta''/\zeta P)\,dy = -(1/12) \cdot \left[d^2\left(\int_{y^1(b)+\delta}^{y^2(b)-\delta}\left((\chi')^2/(b-\chi(y))^{1/2}\right)dy \right)/db^2 \right]_{b=b_n^{(1)}} + O(\delta). \tag{A.11}$$

From (A.10) and (A.11), and the limiting process $k\to\infty$ and $\delta\to 0$, we have the formula (7).

Acknowledgment

The author expresses his thanks to Prof. Yasuura of Kyushu University for his stimulating encouragement. He also wishes to thank Prof. Hashimoto of Osaka Electro-Communication University for his helpful suggestions.

References

[1] D. Gloge and E. A. J. Marcatili, "Impulse response of fibers with ring-shaped parabolic index distribution," *Bell Syst. Tech. J.*, vol. 52, pp. 1161–1168, 1973.

[2] ——,"Multimode theory of graded-core fibers," *Bell Syst. Tech. J.*, vol. 52, pp. 1563–1578, 1973.

[3] M. Hashimoto, "A perturbation method for analysis of wave propagation in inhomogeneous dielectric waveguides with perturbed media," *IEEE Trans. Microwave Theory Tech.*, vol. MTT-24, pp. 559–566, 1976.

[4] E. M. Conwell, "WKB approximation for optical guide modes in a medium with exponentially varying index," *J. Appl. Phys.*, vol. 46, p. 1407, (Communications) 1975.

[5] G. Stewart, C. A. Millar, P. J. R. Laybourn, C. D. W. Wilkinson, and R. M. DeLaRue, "Planar optical waveguides formed by silver-ion migration in glass," *IEEE J. Quantum Electron.*, vol. QE-13, pp. 192–200, 1977.

[6] K. Okamoto and T. Okoshi, "Analysis of wave propagation in optical fibers having core with α-power refractive-index distribution and uniform cladding," *IEEE Trans. Microwave Theory Tech.*, vol. MTT-24, pp. 416–421, 1976.

[7] V. P. Maslov, *Teoria Vozmushchenij i Asimptoticheskije Metody*. Moscow, USSR: Moscow Univ. Press, 1965, pt. II, paragraph 9.

[8] P. M. Morse and H. Feshbach, *Method of Theoretical Physics, Part II*. New York: McGraw-Hill, 1953, pp. 1092–1103.

[9] M. Hashimoto, "The effect of an outer layer on propagation in a parabolic-index optical waveguide," *Int. J. Electron.*, vol. 39, pp. 579–582, 1975.

The Electromagnetic Fields and the Phase Constants of Dielectric Image Lines

KLAUS SOLBACH AND INGO WOLFF

***Abstract*—A method is described for the exact calculation of the field distributions and the phase constants of single and coupled dielectric image lines of rectangular cross section. Field distributions and phase constants calculated by this method are presented as well as experimental results from lines fabricated of paraffin wax. The physical properties of the electromagnetic fields and the mode designation are discussed. The theory is compared to approximate calculation methods known from the literature.**

I. Introduction

DIELECTRIC IMAGE LINES are used as a basis of integrated millimeter-wave circuits; it is hoped that they will solve the problems which are known in connection with the application of microstrip lines in the millimeter-wave range. Therefore, more attention has been paid to this kind of microwave guide in the last five years by several authors; furthermore, the dielectric waveguide has been proposed for application in the optical range. Papers by Goell [1] and Marcatili [2], which are based on investigations by Schlosser and Unger [3], shall be mentioned here. Goell and Marcatili have examined rectangular dielectric waveguides embedded in a second dielectric material; Goell calculated the waveguides by expanding the fields into cylindrical eigensolutions, whereas Marcatili described an approximate solution which was found to neglect the electromagnetic fields of certain field regions. Toulios and Knox [4] in 1970 applied the solutions of Marcatili to the problem of the dielectric image line and showed the possible applications of the line for millimeter wave techniques. Goell [1] only gave the solution of the field problem of one single line; Marcatili described an approximate solution for two coupled lines, which in a similar way has been used by Toulios and Knox. A paper by Levige, Itoh, and Mittra [5] was also based on Marcatili's fundamental approximation method.

In this paper an exact solution is presented for the calculation of the phase constant and the field distributions of one single or two coupled dielectric image lines of rectangular cross section. The method presented can be

Manuscript received January 3, 1977; revised June 10, 1977. This work was supported by the German Research Society under contract Wo 137/2.

The authors are with the Department of Electrical Engineering, University of Duisburg, Duisburg, Germany.

0018-9480/78/0400-0266$00.75

used directly for the calculation of the dielectric image line; it avoids the approximations made by Marcatili. Furthermore, it makes it possible to discuss the physical structure of the electromagnetic waves on single and coupled image lines using the calculated field distributions, and it makes it possible to compute the exact attenuation constant due to dielectric losses in the lines (to be discussed in a future paper).

II. The Calculation Method

In Fig. 1 the investigated waveguide is shown; it consists of two coupled image lines of rectangular cross section. The two lines of width $2w$ and height h are separated by a distance c; they are mounted on a metal ground plane. To define a proper eigenvalue problem, a second metal plate of infinite conductivity is placed at a distance d parallel to the ground plane. The influence of this plate on the properties of the lines can be omitted by choosing a large distance d.

Because of the symmetry of the structure, an even and an odd mode can propagate on the coupled lines. The symmetry plane between the lines is a magnetic wall in the case of the even mode and an electric wall in the case of the odd mode; it means that the structure to be calculated can be reduced to that shown in Fig. 2, where the plane $x=b$ is a magnetic wall in the case of the even mode and an electric wall in the case of the odd mode. If the properties of the single uncoupled line are to be calculated, the limitation $b\to\infty$ is considered; under this condition the two lines shown in Fig. 1 no longer influence each other.

For the calculation of the electromagnetic fields which are possible on a line as shown in Fig. 2, the field region is subdivided into four partial regions (I–IV), and a complete set of field solutions is derived for each subarea. It is assumed that the dependence of the field components on the z coordinate can be described by an exponential function $\exp(-j\beta z)$, β being the phase constant. The x and y dependences of the fields in the regions II, III, and IV are formulated using harmonic functions, so that the boundary conditions are fulfilled on the defined boundaries. In region I it is assumed that the x dependence of the fields can be given by an exponential decay, whereas the y dependences are described by a harmonic function again. The following field potential functions especially have been found for the four regions.

Region I

$$\Pi_1^y = \sum_{\nu=0}^{n} E_\nu \exp\left(\beta_{x\nu}^{(1)}(x+w)\right)\cos\left(\beta_{y\nu}^{(1)}y\right) \tag{1}$$

$$\Lambda_1^y = \sum_{\mu=0}^{n} F_\mu \exp\left(\tilde{\beta}_{x\mu}^{(1)}(x+w)\right)\sin\left(\tilde{\beta}_{y\mu}^{(1)}y\right). \tag{2}$$

Region II

$$\Pi_2^y = \sum_{\nu=1}^{m} \left\{A_\nu \sin\left(\beta_{x\nu}^{(2)}x\right) + A_\nu' \cos\left(\beta_{x\nu}^{(2)}x\right)\right\} \cdot\cos\left(\beta_{y\nu}^{(2)}(y-d)\right) \tag{3}$$

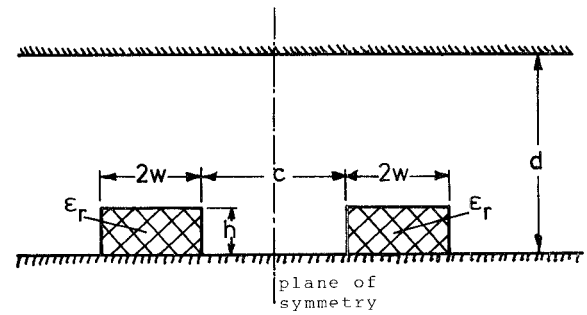

Fig. 1. The cross section of the investigated coupled dielectric image lines.

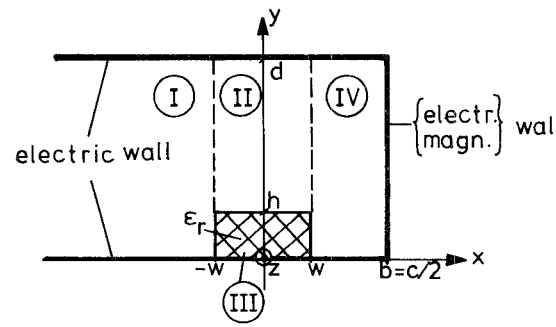

Fig. 2. The cross sectional structure adopted for the calculation of phase constant and field distribution of coupled dielectric image lines.

$$\Lambda_2^y = \sum_{\mu=1}^{m} \left\{B_\mu \cos\left(\tilde{\beta}_{x\mu}^{(2)}x\right) + B_\mu' \sin\left(\tilde{\beta}_{x\mu}^{(2)}x\right)\right\} \cdot\sin\left(\tilde{\beta}_{y\mu}^{(2)}(y-d)\right). \tag{4}$$

Region III

$$\Pi_3^y = \sum_{\nu=1}^{M} \left\{C_\nu \sin\left(\beta_{x\nu}^{(3)}x\right) + C_\nu' \cos\left(\beta_{x\nu}^{(3)}x\right)\right\} \cos\left(\beta_{y\nu}^{(3)}y\right) \tag{5}$$

$$\Lambda_3^y = \sum_{\mu=1}^{M} \left\{D_\mu \cos\left(\tilde{\beta}_{x\mu}^{(3)}x\right) + D_\mu' \sin\left(\tilde{\beta}_{x\mu}^{(3)}x\right)\right\} \sin\left(\tilde{\beta}_{y\mu}^{(3)}y\right). \tag{6}$$

Region IV, Electric Wall at $x=b$

$$\Pi_4^y = \sum_{\nu=0}^{N} G_\nu \sin\left(\beta_{x\nu}^{(4)}(x-b)\right)\cos\left(\beta_{y\nu}^{(4)}y\right) \tag{7}$$

$$\Lambda_4^y = \sum_{\mu=0}^{N} H_\mu \cos\left(\tilde{\beta}_{x\mu}^{(4)}(x-b)\right)\sin\left(\tilde{\beta}_{y\mu}^{(4)}y\right). \tag{8}$$

Region IV, Magnetic Wall at $x=b$

$$\Pi_4^y = \sum_{\nu=0}^{N} G_\nu \cos\left(\beta_{x\nu}^{(4)}(x-b)\right)\cos\left(\beta_{y\nu}^{(4)}y\right) \tag{9}$$

$$\Lambda_4^y = \sum_{\mu=0}^{N} H_\mu \sin\left(\tilde{\beta}_{x\mu}^{(4)}(x-b)\right)\sin\left(\tilde{\beta}_{y\mu}^{(4)}y\right). \tag{10}$$

From the potential functions, the field components can be derived using well-known methods (e.g., [7]). In

(1)–(10) $\beta_x^{(k)}$ and $\beta_y^{(k)}$ $(k=1,2,3,4)$ are the wavenumbers for the TM^y-modes of the regions I–IV, and $\tilde{\beta}_x^{(k)}$ and $\tilde{\beta}_y^{(k)}$ $(k=1,2,3,4)$ are the corresponding wavenumbers of the TE^y-modes. The equations describe a complete solution for the fields if n, m, N, and M become infinite. The following relations hold:

$$k_0^2=\beta^2-\beta_x^{(1)2}+\beta_y^{(1)2}=\beta^2-\tilde{\beta}_x^{(1)2}+\tilde{\beta}_y^{(1)2} \tag{11}$$

$$k_0^2=\beta^2+\beta_x^{2(2)}+\beta_y^{(2)2}=\beta^2+\tilde{\beta}_x^{(2)2}+\tilde{\beta}_y^{(2)2} \tag{12}$$

$$k_0^2\epsilon_r=\beta^2+\beta_x^{(3)2}+\beta_y^{(3)2}=\beta^2+\tilde{\beta}_x^{(3)2}+\tilde{\beta}_y^{(3)2} \tag{13}$$

$$k_0^2=\beta^2+\beta_x^{(4)2}+\beta_y^{(4)2}=\beta^2+\tilde{\beta}_x^{(4)2}+\tilde{\beta}_y^{(4)2} \tag{14}$$

$$k_0^2=\epsilon_0\mu_0\omega^2, \qquad \omega=2\pi f.$$

Because of the boundary conditions at the metallic walls, the following equations result:

$$\beta_{y\nu}^{(1)}=\frac{\nu\pi}{d}, \qquad \nu=0,1,2,\cdots \tag{15}$$

$$\beta_{y\nu}^{(4)}=\frac{\nu\pi}{d}, \qquad \nu=0,1,2,\cdots \tag{16}$$

$$\tilde{\beta}_{y\mu}^{(1)}=\frac{\mu\pi}{d}, \qquad \mu=0,1,2,\cdots \tag{17}$$

$$\tilde{\beta}_{y\mu}^{(4)}=\frac{\mu\pi}{d}, \qquad \mu=0,1,2,\cdots. \tag{18}$$

The boundary conditions in the plane $y=h$, $-w\leqslant x\leqslant +w$ between regions II and III can be fulfilled independently of the remaining conditions. Furthermore, it is possible to match the fields of the TE^y-modes and the TM^y-modes as well as the fields which are even and odd corresponding to the plane $x=0$, separately, on this boundary. From the continuity condition for the tangential electric and magnetic field strength of the TM^y-modes and from a simple coefficient comparison, the following relations result:

$$\beta_{x\nu}^{(2)}=\beta_{x\nu}^{(3)}=\beta_{x\nu} \tag{19a}$$

$$\left.\begin{aligned} A_\nu\beta_{y\nu}^{(2)}\sin\left(\beta_{y\nu}^{(2)}(y-d)\right)&=C_\nu\beta_{y\nu}^{(3)}\sin\left(\beta_{y\nu}^{(3)}h\right)\\ A_\nu\cos\left(\beta_{y\nu}^{(2)}(h-d)\right)&=\epsilon_r C_\nu\cos\left(\beta_{y\nu}^{(3)}h\right).\end{aligned}\right\} \tag{19b}$$

A relation identical to (19b) follows for the dependence between A_ν' and C_ν'. From (19b) the following relation can be derived

$$\tan\left(\beta_{y\nu}^{(2)}(h-d)\right)=\frac{\beta_{y\nu}^{(3)}}{\epsilon_r\beta_{y\nu}^{(2)}}\tan\left(\beta_{y\nu}^{(3)}h\right). \tag{20}$$

In the same manner, equivalent relations are found for the TE^y-modes

$$\tilde{\beta}_{x\mu}^{(2)}=\tilde{\beta}_{x\mu}^{(3)}=\tilde{\beta}_{x\mu} \tag{21a}$$

$$\left.\begin{aligned} B_\mu\sin\left(\tilde{\beta}_{y\mu}^{(2)}(h-d)\right)&=D_\mu\sin\left(\tilde{\beta}_{y\mu}^{(3)}h\right)\\ B_\mu\tilde{\beta}_{y\mu}^{(2)}\cos\left(\tilde{\beta}_{y\mu}^{(2)}(h-d)\right)&=D_\mu\tilde{\beta}_{y\mu}^{(3)}\cos\left(\tilde{\beta}_{y\mu}^{(3)}h\right)\end{aligned}\right\} \tag{21b}$$

$$\tan\left(\tilde{\beta}_{y\mu}^{(2)}(h-d)\right)=\frac{\tilde{\beta}_{y\mu}^{(2)}}{\tilde{\beta}_{y\mu}^{(3)}}\tan\left(\tilde{\beta}_{y\mu}^{(3)}h\right). \tag{22}$$

Analogous equations result from the dependences between B_μ' and D_μ'.

Using the identities $\beta_{x\nu}^{(2)}=\beta_{x\nu}^{(3)}$ and $\tilde{\beta}_{x\mu}^{(2)}=\tilde{\beta}_{x\mu}^{(3)}$, the wavenumbers of the regions II and III can be found independently of the remaining boundary conditions; they are real or imaginary for the field region II, and they are purely real for the fields in region III.

Using the solutions for the wavenumbers, the relations between the amplitude coefficients A_ν and C_ν, B_μ and D_μ, as well as between A_ν' and C_ν', B_μ' and D_μ' can be found from (19b) and (21b), thereby reducing the number of unknown amplitude coefficients by the factor two.

If the boundary conditions in the plane $x=-w$ $(0\leqslant y\leqslant d)$ and $x=+w$ $(0\leqslant y\leqslant d)$ are to be fulfilled, all modes have to be taken into account. It means that from the continuity condition for the E_y and E_z components as well as for the H_y and H_z components, the following relations can be deduced:

$$\beta E_m^{(1)}-\beta_{xm}^{(1)}F_m^{(1)}=\sum_{\nu=1}^{N}\beta A_\nu^{(1)}P_\nu(m)-\sum_{\mu=1}^{N}\tilde{\beta}_{x\mu}B_\mu^{(1)}Q_\mu(m), \qquad m=1,2,\cdots,N-1 \tag{23}$$

$$\epsilon_m(\beta_{xm}^{(1)}E_m^{(2)}-\beta F_m^{(2)})=\sum_{\nu=1}^{N}\beta_{x\nu}A_\nu^{(2)}R_\nu(m)-\sum_{\mu=1}^{N}\beta B_\mu^{(2)}S_\mu(m), \qquad m=0,1,2,\cdots,N-1 \tag{24}$$

$$\epsilon_m(\beta^2-\beta_{xm}^{(1)2})\frac{d}{2}E_m=\sum_{\nu=1}^{N}(\beta^2+\beta_{x\nu}^2)A_\nu^{(1)}T_\nu(m), \qquad m=0,1,2,\cdots,N-1 \tag{25}$$

$$(\beta^2-\tilde{\beta}_{xm}^{(1)2})\frac{d}{2}F_m=\sum_{\mu=1}^{N}(\beta^2+\tilde{\beta}_{x\mu}^2)B_\mu^{(2)}Q_\mu(m), \qquad m=1,2,\cdots,N-1 \tag{26}$$

$$\beta G_m^{(1)}-\beta_{xm}^{(4)}H_m^{(1)}=\sum_{\nu=1}^{N}\beta A_\nu^{(3)}P_\nu(m)-\sum_{\mu=1}^{N}\tilde{\beta}_{x\mu}B_\mu^{(3)}Q_\mu(m), \qquad m=1,2,\cdots,N-1 \tag{27}$$

$$\epsilon_m(\beta_{xm}^{(4)}G_m^{(2)}-\beta H_m^{(2)})=\sum_{\nu=1}^{N}\beta_{x\nu}A_\nu^{(4)}R_\nu(m)-\sum_{\mu=1}^{N}\beta B_\mu^{(4)}S_\mu(m), \qquad m=0,1,2,\cdots,N-1 \tag{28}$$

$$\epsilon_m(\beta^2+\beta_{xm}^{(4)2})\frac{d}{m\pi}G_m^{(1)}=\sum_{\nu=1}^{N}(\beta^2+\beta_{x\nu}^2)A_\nu^{(3)}T_\nu(m), \qquad m=0,1,2,\cdots,N-1 \tag{29}$$

$$(\beta^2+\beta_{xm}^{(4)2})\frac{d}{m\pi}H_m^{(2)}=\sum_{\mu=1}^{N}(\beta^2+\tilde{\beta}_{x\mu}^2)B_\mu^{(4)}Q_\mu(m), \qquad m=1,2,\cdots,N-1 \tag{30}$$

$$\epsilon_m = \begin{cases} 1, & \text{if } m \neq 0 \\ 2, & \text{if } m = 0. \end{cases}$$

$P_\nu(m)$, $Q_\mu(m)$, $R_\nu(m)$, $S_\mu(m)$, and $T_\nu(m)$ are coupling integrals, as they can be derived through the matching of the fields in the boundaries (see Appendix I). The field matching is achieved so that the mean-square deviation of the field approximations can be made arbitrarily small. The amplitude coefficients in (23)–(30) depend on the originally used amplitude values $A_\nu, \cdots, H_\mu$ and $A'_\nu, \cdots, D'_\mu$ as described in Appendix II.

The number of equations needed to calculate the eigenvalue problem ((23)–(30)) can be reduced if the coefficients E_m and F_m are calculated from (25) and (26) and are inserted into (23) and (24). The same is true for the coefficients G_m and H_m in connection with (27)–(30). If the phase constant of the waves on the dielectric image line is to be computed, the zeros of the determinant of the remaining set of equations must be determined. First, at a given frequency the determinant is examined for its zero crossings for β in the range of β_0 to $\beta_0\sqrt{\epsilon_r}$ by computing its value in determined intervals and comparing it to the preceding one.

The exact values of β are calculated by starting an iterative search for the zero inside the intervals of the zero crossings by means of the Newton method. The search can be conducted on the basis of the real part or the imaginary part of the determinant since the determinant is purely real or purely imaginary piecewise.

The calculation of the determinant was done by employing the Gauss-elimination method. Because in some cases the value of the determinant exceeded the numerical range of the computer, the range of the determinant was reduced by suitable normalization of the coupling integrals $P_\nu(m)$ to $T_\nu(m)$ before starting the search for zero crossings.

From the phase constant β, the wavenumbers, $\beta_{x\nu}$, $\tilde{\beta}_{x\mu}$, $\beta^{(1)}_{x\nu}$, $\tilde{\beta}^{(1)}_{x\mu}$, $\beta^{(4)}_{x\nu}$, and $\tilde{\beta}^{(4)}_{x\mu}$ result. Using the solution of the set of equations, the field potentials (1)–(10) for the four field regions can be derived. From the field potentials the field distributions of the electric and magnetic fields can be calculated.

III. Numerical Results

The eigenvalue equation of one single and two coupled dielectric image lines has been evaluated using a Cyber 76 computer of Control Data Corporation.

In Fig. 10 the phase constant normalized to $k_0 = \omega\sqrt{\epsilon_0 \mu_0}$ is shown for the three lowest order modes on a single dielectric image line. The fundamental EH_{11} mode has no cutoff frequency, whereas the phase constants of the higher order modes do exist only for frequencies higher than a cutoff frequency. At the cutoff frequency β is equal to k_0. Furthermore, a comparison between the results of this theory and that given by Marcatili [2] and Toulios and Knox [4] is shown in Fig. 10. The method of Marcatili or Toulios and Knox has been adapted in order to make its results comparable to the results calculated here.

In the field region between the upper side of the dielectric guide and the metallic shielding, a hyperbolic function is taken into account instead of the exponential function in the original field description in [2] and [4], so that the tangential electric field vanishes at the shielding plate.

The designation of the possible modes on the dielectric image line used in this paper is based on the relationship of the modes on the dielectric image line to those of a simple dielectric slab guide: E(TM) modes having only E_z, E_y, and H_x components and H(TE) modes possessing only H_z, H_y, and E_x components. Thus the modes of the dielectric image line are designated EH if the field strengths E_z, E_y, and H_x are superior to the field strengths H_z, H_y, and E_x. Respectively, they are designated HE if the contrary is true. In agreement with the mode description in [1], indices p and q are introduced to determine the number of maximums of the E_y components in region III in the x and y direction, respectively. In [2] and [4] it is assumed that the E_y and H_x components are much larger than all other field components. This assumption was the basis of Marcatili's approximation.

As can be shown by means of the theory described in this paper, this assumption in general is not valid; the assumption is applicable only to the fundamental modes EH_{11} (Fig. 3 and Fig. 4) or the EH_{11e} and EH_{11o} in case of coupled lines (see Fig. 7) of low permittivity lines ($\epsilon_r \lesssim 3$) and arbitrary aspect ratio w/h. High permittivity lines of very high or very low aspect ratio (degenerated into dielectric slab or dielectric sheet waveguide) can also be described well under the above assumption.

If the field distributions of the magnetic and electric field strength of the EH_{11} fundamental mode on a single low permittivity dielectric image line are calculated, Fig. 3 and Fig. 4 result. Fig. 3 is valid in the case of a relatively low frequency, and Fig. 4 is valid in the case of a relatively high frequency. It can be seen clearly that a remarkable difference exists in the field decay outside the dielectric. For low frequencies a large part of the electromagnetic energy travels in the air region, whereas for higher frequencies the energy is concentrated more and more in the dielectric material. In the planes $x = \pm w$ and $y = h$ the normal component of the electric field strength (E_x for $x = \pm w$, E_y for $y = h$) in agreement with the boundary conditions is not continuous.

The field distribution of the dielectric image line of rectangular cross section with $w \approx h$ is similar to that of the circular dielectric wire. The fundamental mode EH_{11} of the image line corresponds to the "dipole mode" EH_{11} of the circular dielectric waveguide. Both modes converge into a plane wave for low frequencies ($f \to 0$). The next two higher order modes of the image line with the indices $p, q = 2$, and 1 (Fig. 5) correspond to the rotational symmetric modes TE_{10} and TM_{10} of the circular guide. The HE modes of the image line at the same frequency have a lower phase velocity than the EH modes, as is the case with the TE and the TM modes of the circular dielectric guide; the HE_{21}-mode field characteristics are similar to the characteristics of a transversal electric mode, whereas the EH_{21} mode is similar to a transversal magnetic mode. Modes with indices $p, q = 4, 1; 6, 1; 8, 1; \cdots$, in the same

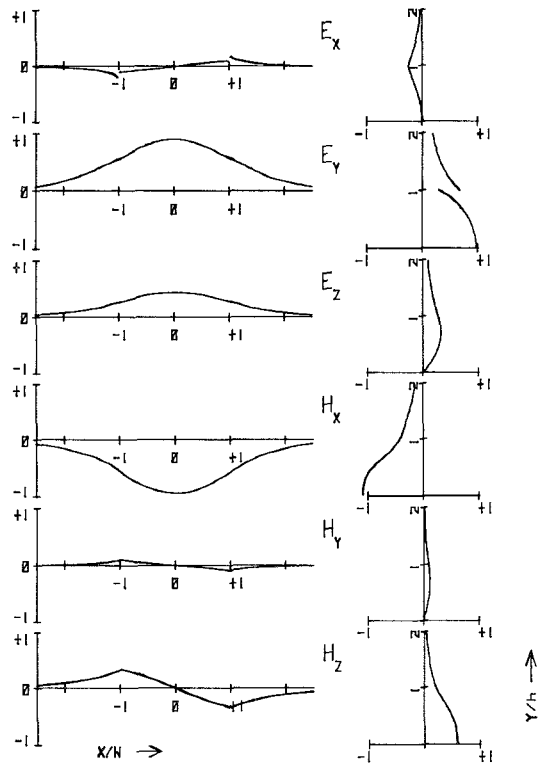

Fig. 3. Normalized calculated field distributions of the EH_{11} mode on a dielectric image line in a horizontal plane at $y=0.8h$ and in a vertical plane at $x=0.9w$. $w/h=1$, $b/w\to\infty$, $d/h\to\infty$, $B=1.2$, $\beta/\beta_0=1.1854$, and $\epsilon_r=2.22$.

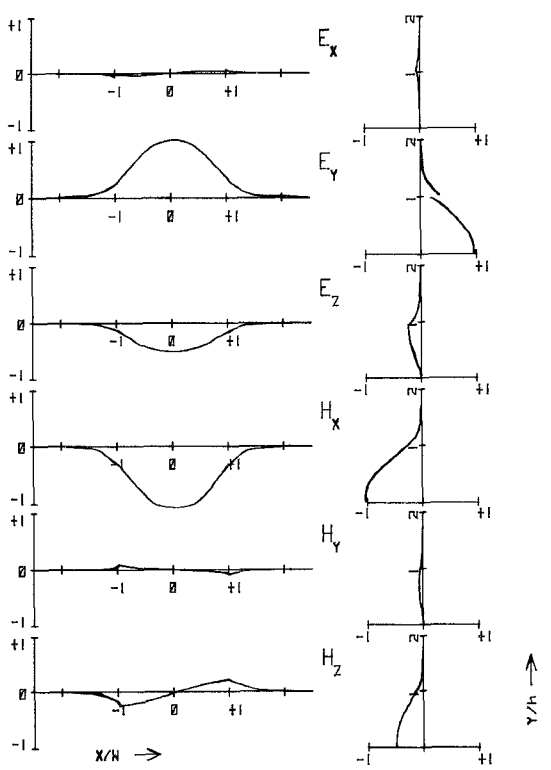

Fig. 4. Normalized calculated field distributions of the EH_{11} mode on a dielectric image line in a horizontal plane at $y=0.8h$ and in a vertical plane at $x=0.9w$. $w/h=1$, $b/w\to\infty$, $d/h\to\infty$, $B=3.0$, $\beta/\beta_0=1.420$, and $\epsilon_r=2.22$.

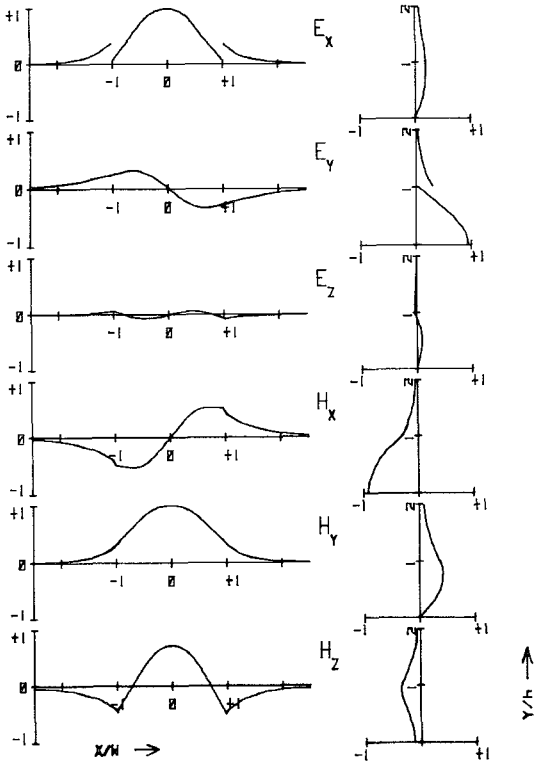

Fig. 5. Normalized calculated field distributions of the HE_{21} mode on a high permittivity dielectric image line in a horizontal plane at $y=0.8h$ and in a vertical plane at $x=0.9w$. $w/h=1$, $b/w\to\infty$, $d/h\to\infty$, $B=2.0$, $\beta/\beta_0=1.9183$, and $\epsilon_r=10$.

manner correspond to the TE_{20}, TM_{20}; TE_{30}, TM_{30}; TE_{40}, TM_{40}; $\cdots$ modes of the circular dielectric guide. All other modes are essentially hybrid modes like the fundamental mode EH_{11}; under certain restrictions they correspond to the remaining modes EH_{22}, HE_{22}, $EH_{31}, HE_{31}, \cdots$ of the circular dielectric guide.

In Fig. 6 the field distribution of an image line of large width w are shown. The electromagnetic field is concentrated for the greater part in the dielectric medium. The fields correspond very closely to those of the dielectric slab guide which supports TE_m and TM_m modes. The fundamental mode TM_0 for low frequencies converges into a plane wave; a TE_0 mode is not supported. As can be seen from Fig. 6, the fundamental mode EH_{11} of the dielectric image line is nearly transversely magnetic. The modes of the image line with indices $p=1,2,3,\cdots$ and $q=1$ correspond to the TM_p modes of the dielectric slab guide. The modes with $p=1,2,3,\cdots$ and $q=2,3,4,\cdots$ may be divided into two groups with TE or TM characteristics, respectively; they correspond to the TE or TM modes of the dielectric slab guide and are called HE_{pq} and EH_{pq} modes, respectively.

Analogous to the above discussion, dielectric image guides of large height h can be compared to the dielectric sheet; the restriction has to be made that only those modes of the dielectric sheet which have no electric field component in the z–x plane are compared to the modes of the dielectric image line. These are the even and odd TE and TM modes, of which only the TE_0 mode has no

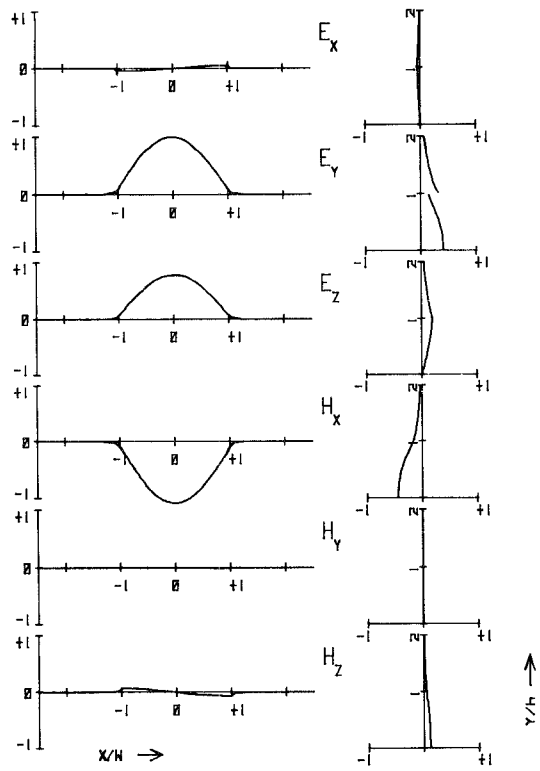

Fig. 6. Normalized calculated field distributions of the EH_{11} mode on a flat dielectric image line in a horizontal plane at $y=0.8h$ and in a vertical plane at $x=0.9w$. $w/h=10$, $b/w\to\infty$, $d/h\to\infty$, $B=1.25$, $\beta/\beta_0=1.3183$, and $\epsilon_r=2.22$.

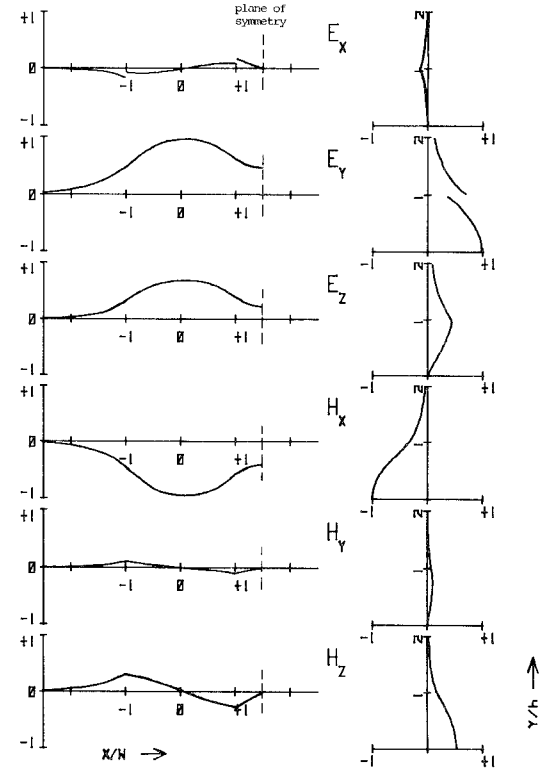

Fig. 7. Normalized calculated field distributions of the EH_{11e} mode on coupled dielectric image lines in a horizontal plane at $y=0.8h$ and in a vertical plane at $x=0.9w$. $w/h=1$, $b/w=1.5$, $d/h\to\infty$, $B=1.5$, $\beta/\beta_0=1.2756$, and $\epsilon_r=2.22$.

cutoff frequency. For a very low aspect ratio w/h ($w/h\to 0$), the fundamental mode EH_{11} of the dielectric image line converges into this mode. Besides analogous results to those found by the comparison of the flat image line with the dielectric slab guide are valid for the narrow image line in correspondence to the dielectric sheet guide.

In Fig. 5 the field distributions of a HE_{21} mode on a high permittivity image line ($\epsilon_r=10$) is shown. The step of the normal electric field strength on the dielectric interfaces is very large.

In Fig. 7 the fields of the even mode of two coupled image lines with $w/h=1$ and $b/w=1.5$ are plotted. The E_y, E_z, and H_x components do not become zero in the plane of symmetry, whereas the E_x, H_y, and H_z components vanish; this is equivalent to a magnetic wall in the plane of symmetry.

The calculated values of the phase constant of single and coupled dielectric image lines are not only dependent on the geometrical and electrical parameters of the lines but also on the number N of the field modes which have been taken into account in the calculation procedure. The problem of relative convergence does not appear due to the fact that the fields near the edges of the guide ($x=\pm w$, $y=h$) remain finite. Furthermore, the adopted shielding plate may have an influence on the transmission properties of the line. A minimum value of height d which is dependent on the frequency and the dielectric constant can be found so that the error caused by the shielding is negligibly small. As Fig. 8 and Fig. 9 show, the influence of the number of field modes on the computed results is very small. For many applications, a solution which only considers two field modes can be good enough. As a general rule, it can be concluded that the height d may become smaller with increasing frequency, and that the number of field modes considered must become larger with increasing height d in order to reject the influences of these values on the computed phase constant.

It is necessary that the number of field modes considered is much larger than the quotient d/h if the field distributions are to be calculated, especially if the discontinuities of the normal electric field components are to be computed with satisfying accuracy. For example, if $d/h=5$, N has to be at least 15 to get a satisfying field description.

In Figs. 10–14 the normalized phase constant β/β_0 is shown versus the frequency f normalized to the cutoff frequency of the first higher order mode (TE_1) of a dielectric slab guide, which is of the same height h and dielectric constant ϵ_r as the dielectric image line. As can be seen from Figs. 10–14, the approximation given by Toulios and Knox [4] in the case of rather low permittivity lines is quite good, whereas the solution described by Marcatili [2] is not satisfying. The opposite is true for high permittivity lines. This can also be concluded from the comparison of Goell's exact curves for single lines [1] with both approximate theories [2] and [4].

Contrary to the approximate calculation methods, the method described here provides two different solutions for

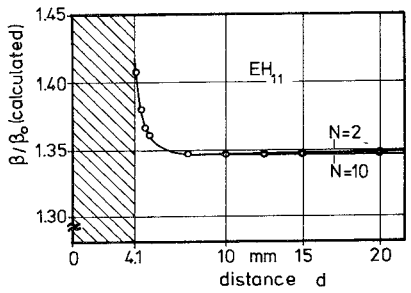

Fig. 8. Calculated phase constant of the EH_{11} mode on a dielectric image line versus the height d of the shielding plate depending on the number N of the field modes considered. $w/h=1$, $b/w\to\infty$, $B=2.0$, and $\epsilon_r=2.22$.

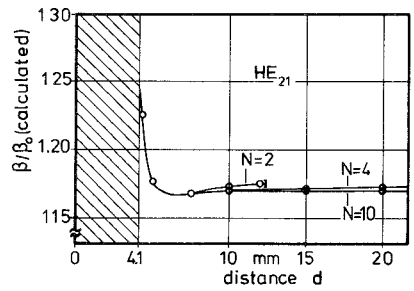

Fig. 9. Calculated phase constant of the HE_{21} mode on a dielectric image line versus the height d of the shielding plate depending on the number N of field modes considered. $w/h=1$, $b/w\to\infty$, $B=2.0$, and $\epsilon_r=2.22$.

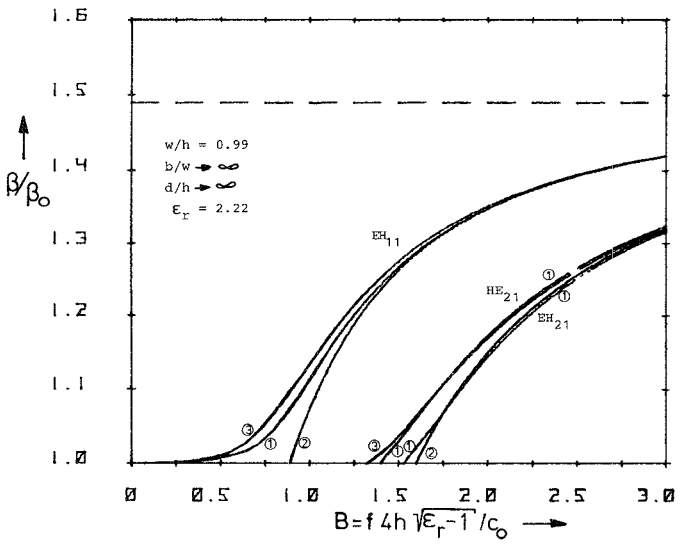

Fig. 10. Normalized phase constant of a dielectric image line versus the normalized frequency B. (1) This theory, (2) Marcatili's approximation [2], (3) approximation of Toulios and Knox [4].

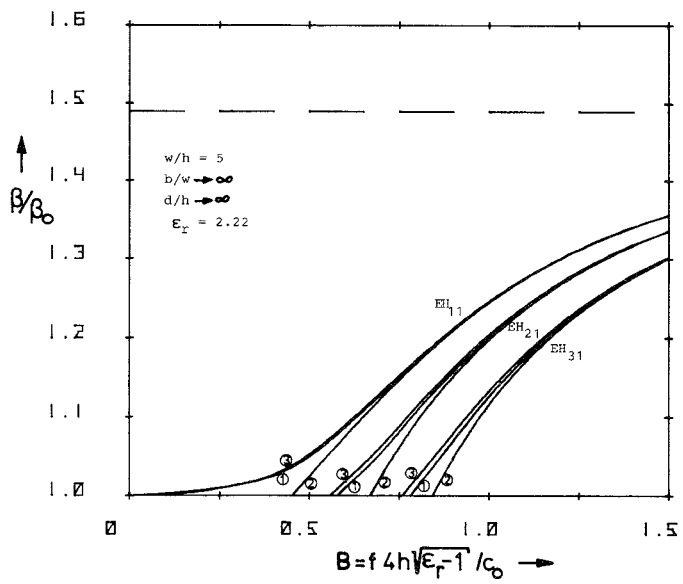

Fig. 11. Normalized phase constant of a flat dielectric image line versus the normalized frequency B. (1) This theory, (2) Marcatili's approximation [2], (3) approximation of Toulios and Knox [4].

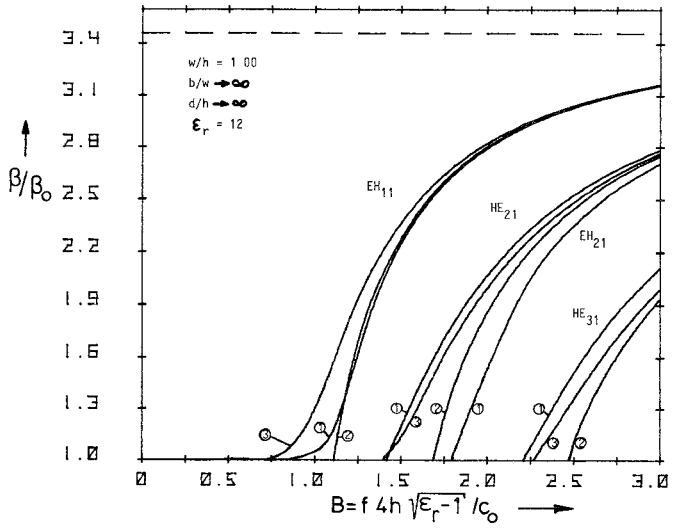

Fig. 12. Normalized phase constant of a high permittivity dielectric image line versus the normalized frequency B. (1) This theory, (2) Marcatili's approximation [2], (3) approximation of Toulios and Knox [4].

certain sets of indices, for example, for $p,q=2,1$, the EH_{21}, and the HE_{21} modes. Only one of these solutions is approximated by the approximate theories of Toulios, Knox, and Marcatili.

In Fig. 11 the phase constant of a flat dielectric image line is plotted; in this case the approximation after [4] is in very good agreement with our method. This is true for the fundamental mode as well as for the higher modes.

In Fig. 13 and Fig. 14 the normalized phase constants of the even and the odd mode of two coupled low permittivity dielectric image lines are shown. Even in this case it can be stated that solutions exist which cannot be calculated using the approximate methods. Those modes which are a solution to the theory of Toulios and Knox, are approximated quite well by their method.

IV. Measurement Results

The theoretical results for field distributions as well as for phase constants have been proven experimentally. The experimental method and some measurement results of field distributions have been described in [6]. In Fig. 15 and Fig. 16 the measured and calculated phase constants are compared. The agreement between theory and experiment is very good. Decisive discrepances between theory and experiment could be measured in no case. It can be seen from Fig. 15 especially that the additional solution of

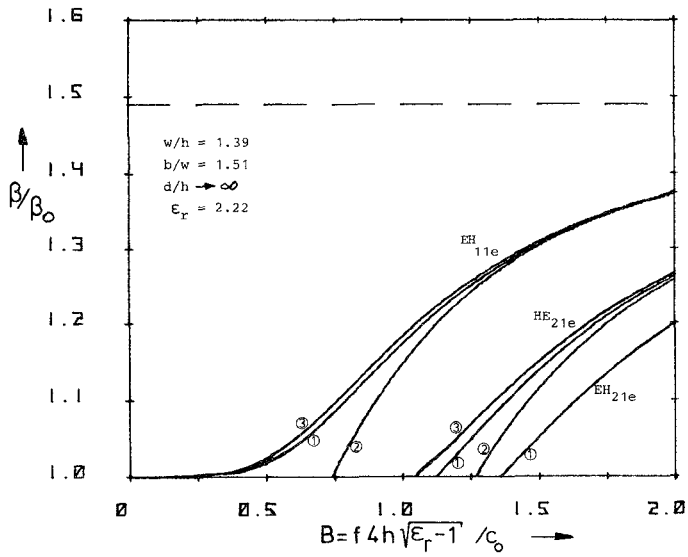

Fig. 13. Normalized phase constant of the even modes on two coupled dielectric image lines versus the normalized frequency B. ① This theory, ② Marcatili's approximation [2], ③ approximation of Toulios and Knox [4].

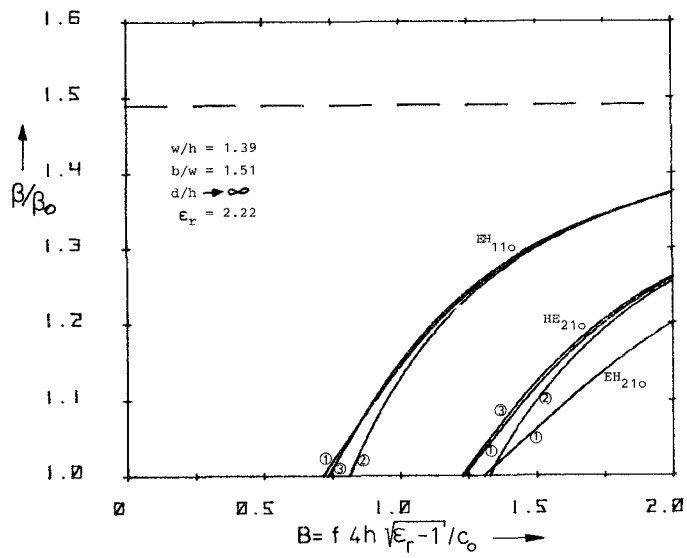

Fig. 14. Normalized phase constant of the odd modes on two coupled dielectric image lines versus the normalized frequency B. ① This theory, ② Marcatili's approximation [2], ③ approximation of Toulios and Knox [4].

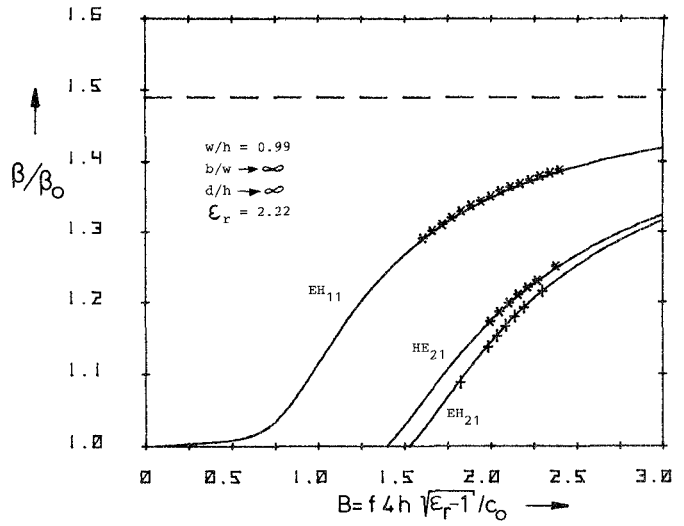

Fig. 15. Normalized phase constant of a dielectric image line versus the normalized frequency B. ——— This theory, + and * experimental data from lines of height $h = 4.1$ mm.

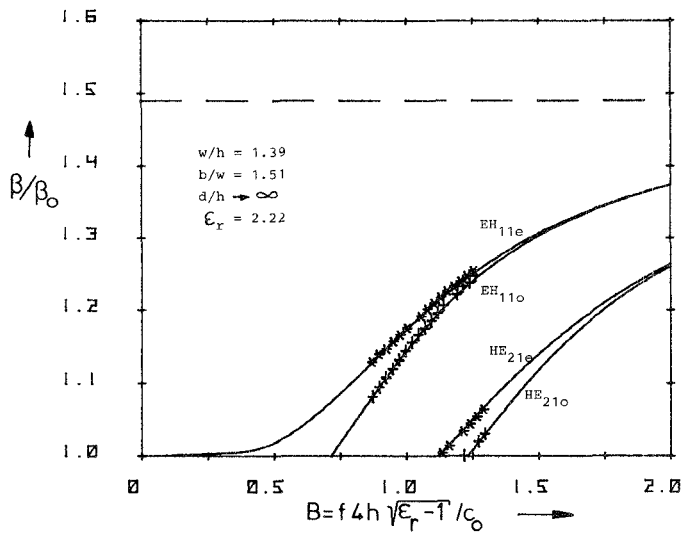

Fig. 16. Normalized phase constant of the even and odd mode on two coupled dielectric image lines versus the normalized frequency B. ——— This theory, * and + experimental data from lines of height $h = 2.2$ mm.

the EH_{21} mode could be measured very clearly. Therefore, it results that the theory presented here can be accepted as a reliable instrument to calculate the properties of the dielectric image line exactly. Furthermore, because the computing time needed for the calculation of one frequency-dependent phase constant is small ($t < 1s$ on a Cyber 76), the method presented is efficient too.

Appendix I

Coupling Integrals

$$I_1(m) = \int_0^h \sin\left(\beta_{y\nu}^{(3)} y\right) \sin\left(\frac{m\pi}{d} \cdot y\right) dy$$

$$I_2(m) = \int_0^h \cos\left(\beta_{y\nu}^{(3)} y\right) \cos\left(\frac{m\pi}{d} \cdot y\right) dy$$

$$I_3(m) = \int_h^d \sin\left(\beta_{y\nu}^{(2)}(y-d)\right) \sin\left(\frac{m\pi}{d} \cdot y\right) dy$$

$$I_4(m) = \int_h^d \cos\left(\beta_{y\nu}^{(2)}(y-d)\right) \cos\left(\frac{m\pi}{d} \cdot y\right) dy$$

$$\tilde{I}_1(m) = \int_0^h \sin\left(\beta_{y\mu}^{(3)} y\right) \sin\left(\frac{m\pi}{d} \cdot y\right) dy$$

$$\tilde{I}_2(m) = \int_0^h \cos\left(\beta_{y\mu}^{(3)} y\right) \cos\left(\frac{m\pi}{d} \cdot y\right) dy$$

$$\tilde{I}_3(m) = \int_h^d \sin\left(\beta_{y\mu}^{(2)}(y-d)\right) \sin\left(\frac{m\pi}{d} \cdot y\right) dy$$

$$\tilde{I}_4(m) = \int_h^d \cos\left(\beta_{y\mu}^{(2)}(y-d)\right) \cos\left(\frac{m\pi}{d} \cdot y\right) dy.$$

$$P_\nu(m) = \beta_{y\nu}^{(3)} k_\nu^{C-A} I_1(m) + \beta_{y\nu}^{(2)} I_3(m)$$

$$Q_\mu(m) = k_\mu^{D-B} \tilde{I}_1(m) + \tilde{I}_3(m)$$

$$R_\nu(m) = \epsilon_r k_\nu^{C-A} I_2(m) + I_4(m)$$

$$S_\mu(m) = \tilde{\beta}^{(3)}_{y\mu} k_\mu^{D-B} \tilde{I}_2(m) + \beta^{(2)}_{y\mu} \tilde{I}_4(m)$$

$$T_\nu(m) = k_\nu^{C-A} I_2(m) + I_4(m)$$

with

$$k_\nu^{C-A} = \frac{\cos\left(\beta^{(2)}_{y\nu}(h-d)\right)}{\cos\left(\beta^{(3)}_{y\nu} h\right)} / \epsilon_r \text{ and}$$

$$k_\mu^{D-B} = \frac{\sin\left(\tilde{\beta}^{(2)}_{y\mu} \cdot (h-d)\right)}{\sin\left(\tilde{\beta}^{(3)}_{y\mu} \cdot h\right)}.$$

Appendix II

Amplitude Coefficients

$$E_m^{(1)} = \frac{m\pi}{2} E_m$$

$$F_m^{(1)} = \frac{d}{2} \omega\mu_0 F_m$$

$$A_\nu^{(1)} = -A_\nu \sin\left(\beta_{x\nu} \cdot w\right) + A'_\nu \cos\left(\beta_{x\nu} \cdot w\right)$$

$$B_\mu^{(1)} = \mu_0\omega\left[B_\mu \cdot \sin\left(\tilde{\beta}_{x\mu} \cdot w\right) + B'_\mu \cdot \cos\left(\tilde{\beta}_{x\mu} \cdot w\right)\right]$$

$$E_m^{(2)} = \omega\epsilon_0 \frac{d}{2} E_m$$

$$F_m^{(2)} = \frac{m\pi}{2} F_m$$

$$A_\nu^{(2)} = \omega\epsilon_0\left[A_\nu \cdot \cos\left(\beta_{x\nu} \cdot w\right) + A'_\nu \cdot \sin\left(\beta_{x\nu} \cdot w\right)\right]$$

$$B_\mu^{(2)} = B_\mu \cdot \cos\left(\tilde{\beta}_{x\mu} \cdot w\right) - B'_\mu \cdot \sin\left(\tilde{\beta}_{x\mu} \cdot w\right)$$

$$A_\nu^{(3)} = A_\nu \cdot \sin\left(\beta_{x\nu} \cdot w\right) + A'_\nu \cdot \cos\left(\beta_{x\nu} \cdot w\right)$$

$$B_\mu^{(3)} = \omega\mu_0\left[-B_\mu \cdot \sin\left(\tilde{\beta}_{x\mu} \cdot w\right) - B_\mu \cdot \cos\left(\beta_{x\mu} \cdot w\right)\right]$$

$$A_\nu^{(4)} = \omega\epsilon_0\left[A_\nu \cos\left(\beta_{x\nu} \cdot w\right) - A'_\nu \sin\left(\beta_{x\nu} \cdot w\right)\right]$$

$$B_\mu^{(4)} = B_\mu \cdot \cos\left(\tilde{\beta}_{x\mu} \cdot w\right) + B'_\mu \cdot \sin\left(\tilde{\beta}_{x\mu} \cdot w\right).$$

In Case of an Electric Wall at $x = b$

$$G_m^{(1)} = \frac{m\pi}{2} \sin\left(\beta^{(4)}_{xm}(w-b)\right) G_m$$

$$H_m^{(1)} = -\frac{d}{2} \omega\mu_0 \sin\left(\beta^{(4)}_{xm}(w-b)\right) H_m$$

$$G_m^{(2)} = \frac{d}{2} \omega\epsilon_0 \cos\left(\beta^{(4)}_{xm}(w-b)\right) G_m$$

$$H_m^{(2)} = \frac{m\pi}{2} \cos\left(\beta^{(4)}_{xm}(w-b)\right) H_m.$$

In Case of a Magnetic Wall at $x = b$

$$G_m^{(1)} = \frac{m\pi}{2} \cos\left(\beta^{(4)}_{xm}(w-b)\right) G_m$$

$$H_m^{(1)} = \frac{d}{2} \omega\mu_0 \cos\left(\beta^{(4)}_{xm}(w-b)\right) H_m$$

$$G_m^{(2)} = -\frac{d}{2} \omega\epsilon_0 \sin\left(\beta^{(4)}_{xm}(w-b)\right) G_m$$

$$H_m^{(2)} = \frac{m\pi}{2} \sin\left(\beta^{(4)}_{xm}(w-b)\right) H_m.$$

References

[1] J. E. Goell, "A circular-harmonic computer analysis of rectangular dielectric waveguides," *Bell Syst. Tech. J.*, vol. 48, pp. 2133–2160, Sept. 1969.

[2] E. A. J. Marcatili, "Dielectric rectangular waveguide and directional coupler for integrated optics," *Bell Syst. Tech. J.*, vol. 48, pp. 2071–2102, Sept. 1969.

[3] W. Schlosser and H. G. Unger, "Partially filled waveguides and surface waveguides of rectangular cross section," *Advances of Microwaves*, vol. 1. New York: Academic Press, 1966, pp. 319–387.

[4] R. M. Knox and P. P. Toulios, "Integrated circuits for the millimeter through optical frequency range," in *Proc. Symp. Submillimeter Waves*, Polytechnic Press of Polytechnic Institute of Brooklyn, Brooklyn, NY, 1970, pp. 497–516.

[5] W. V. McLevige, T. Itoh, and R. Mittra, "New waveguide structure for millimeter wave and optical integrated circuits," *IEEE Trans. Microwave Theory Tech.*, vol. MTT-23, pp. 788–794, Oct. 1975.

[6] K. Solbach, "The fabrication of dielectric image lines using casting resins and the properties of the lines in the millimeter-wave range," *IEEE Trans. Microwave Theory Tech.*, vol. MTT-24, pp. 879–887, Nov. 1976.

[7] H.-G. Unger, *Elektromagnetische Wellen I.* Braunschweig, Germany: Friedr. Vieweg & Sohn, 1967.